APL Photonics

Thermally stable high numerical aperture integrated waveguides and couplers for the 3 μm wavelength range

Cite as: APL Photonics **7**, 126106 (2022); https://doi.org/10.1063/5.0119961
Submitted: 10 August 2022 • Accepted: 26 November 2022 • Accepted Manuscript Online: 28 November 2022 • Published Online: 12 December 2022

T. Toney Fernandez, B. Johnston, H. Mahmodi, et al.

Thermally stable high numerical aperture integrated waveguides and couplers for the 3 μm wavelength range

Cite as: APL Photon. 7, 126106 (2022); doi: 10.1063/5.0119961
Submitted: 10 August 2022 • Accepted: 26 November 2022 •
Published Online: 12 December 2022

T. Toney Fernandez,[1,a)] B. Johnston,[1] H. Mahmodi,[2] K. Privat,[3] I. Kabakova,[2] S. Gross,[4] M. Withford,[1] and A. Fuerbach[1,b)]

AFFILIATIONS

[1] MQ Photonics Research Centre, School of Mathematical and Physical Sciences, Macquarie University, Macquarie Park, NSW 2109, Australia
[2] School of Mathematical and Physical Sciences, University of Technology Sydney, Ultimo, NSW 2007, Australia
[3] Electron Microscope Unit, Mark Wainwright Analytical Centre, University of New South Wales, Sydney, Australia
[4] School of Engineering, Macquarie University, Macquarie Park, NSW 2109, Australia

[a)] **Electronic mail:** toney.teddyfernandez@mq.edu.au
[b)] **Author to whom correspondence should be addressed:** alex.fuerbach@mq.edu.au

ABSTRACT

The femtosecond laser direct write technique was used to fabricate mid-infrared compatible waveguide couplers into Suprasil 3001, a fused silica glass with an OH content of as low as ≤1 ppm. Smooth positive step-index change multi-scan waveguides were produced with a high index contrast of 1×10^{-2}, measured directly using quadriwave lateral shearing interferometry. Waveguides were annealed at 400 °C for 15 h and found to be highly stable, with only <5% reduction in positive index change. Brillouin microscopy and cathodoluminescence are introduced as novel tools that complement Raman mapping and electron microscopy for the investigation of the laser-induced structural changes within the glass matrix, and it was found that although a uniform step index profile is observed across the entire guiding region, different physical mechanisms underpin the index change in the upper and lower sections of the waveguide cross-section, respectively. Waveguides were optimized for mode-matching with optical fibers for the 3.2 μm wavelength range, and evanescent four-port directional couplers with coupling ratios ranging from 5:95 to 50:50 were designed and fabricated. This demonstration opens the door to the development of fully integrated and temperature-stable hybrid chip/fiber systems for the important mid-infrared spectral range.

I. INTRODUCTION

There is an urgent need for integrated optical components for mid-infrared (mid-IR) wavelengths due to the rapid progress that has been made over the past several years in the generation, detection, and manipulation of light in this highly important wavelength range.[1,2] Fiber-based sources capable of delivering high-energy few-cycle laser pulses in the 3 μm range have recently been demonstrated, yet these systems either rely on the use of bulk optical components[3] or on nonlinear frequency up-conversion from near-infrared sources.[4] While fiber-coupled optical components like couplers and splitters are readily available in the near-infrared, in particular at telecommunications wavelengths, the development of equivalent devices for the important mid-infrared spectral region is proving to be difficult. Since the standard silica glasses are not transparent at these wavelengths, research efforts have concentrated on soft glasses like zirconium fluoride (ZBLAN)[5] and chalcogenides.[6,7]

The femtosecond laser direct write method[8] has been shown to be a powerful and versatile method for the fabrication of fiber-coupled integrated optical components. However, due to the aforementioned material challenge, little emphasis has been placed on mid-infrared compatible materials and most of published work to date has concentrated on highly nonlinear chalcogenide glasses, such as gallium lanthanum sulphide (GLS)[9] or $As_{40}S_{60}$.[10] However,

apart from the high nonlinear refractive index that is a nuisance for many applications, these glasses also have an inherently high linear refractive index, which results in high Fresnel losses when coupling to low-index fluoride fibers.[11] In terms of femtosecond laser waveguide inscription into fluoride glasses, it has been shown that index changes in the low 10^{-3} range[12,13] can be achieved. However, a value of $\Delta n = 3 \times 10^{-3}$ in these glasses corresponds to a numerical aperture (NA) < 0.1, which is not compatible with commercially available mid-infrared fibers, which typically feature NAs in the range 0.1–0.3. Very recently, we demonstrated that the positive index change in fluoride glasses can be increased to 8×10^{-3} by modifying the composition of the bulk glass before fs-laser inscription.[14] In silica glasses, fiber-coupled chips with excellent mode-matching have been demonstrated, yet at shorter wavelengths.[15] Highly temperature-stable waveguides have been femtosecond laser inscribed into sapphire,[16] yet these waveguides were based on a depressed-cladding architecture, which makes it hard to realize more complex devices, such as couplers, and the index change was also limited to about 3.5×10^{-3}. Therefore, a mid-IR transparent low-index material that allows the fabrication of low-loss optical waveguides with high index contrast is needed, as it would make it possible to achieve near-perfect mode matching and therefore efficient coupling to commercially available mid-IR active and passive optical fibers, thus enabling the development of all-integrated hybrid chip-fiber systems for the mid-IR. Suprasil® 3001 fused silica glass, with its ultra-low OH content and thus very low mid-IR absorption, is an ideal candidate as its refractive index (1.4193 at 3.0 μm) is closely matched to that of commercial fluoride fibers (InF_3: 1.4193; ZBLAN: 1.4909 at 3.0 μm, respectively). Suprasil 3001 also features very high thermal and mechanical stability, in particular when compared to soft-glass mid-IR materials, and low nonlinearity and dispersion in the mid-IR comparable to fluoride glasses.[17] A comprehensive overview of the optical (UV to mid-IR), mechanical, and thermal properties of this glass can be found in the data sheet provided by the manufacturer.[18]

II. METHODS

Waveguides of 20 mm length were inscribed using a Light Conversion Pharos femtosecond laser system operating at a central wavelength of 1030 nm and pulse duration of 240 fs. After inscription, waveguides were imaged via differential interference contrast (DIC) microscopy using an Olympus inverted microscope. Full 2-D refractive index profiles were obtained via quadriwave lateral shearing interferometry[19] using a SID4HR camera from Phasics. These measurements were carried out at a wavelength of 600 nm on small waveguide cuboids, which were only 12 μm long. This short thickness ensures that the optical path difference vs refractive index remains within a linear relationship. An exhaustive explanation of the procedure can be found in Abou Khalil *et al.*[20] Mid-infrared waveguide mode profiling was carried out within the 2–3.2 μm wavelength range using a Dataray Wincam S-WCD-IR-BB-30 beam profiler. A structural and chemical characterization of the waveguides was carried out using a JEOL JXA-8500F field-emission electron microprobe and a FEI Nova NanoSEM 450 field-emission scanning electron microscope operating at 10 kV and equipped with a Delmic SPARC spectral cathodoluminescence detection system with a Zyla-VISNIR spectrometer and gratings blazing at 300 and 800 nm. A Renishaw inVia Qontor Raman microscope using 514 nm excitation was used to map the Raman spectra over the waveguide cross-section. The mapping was carried out in confocal mode using a 100× objective, providing a spatial resolution of ≈0.5 μm. Brillouin frequency shifts (BFS) were measured using a 660 nm single-frequency Cobolt Flamenco laser (HÜBNER Photonics) through a confocal microscope (CM1, TableStable Ltd.). The details of BFS measurements can be found in Ref. 14.

III. RESULTS AND DISCUSSION

A. Optimization of index change

Multiscan waveguides[21] were inscribed using six different repetition rates of 100, 250, 375, 500, 750 kHz, and 1 MHz. A 0.6 and a 0.4 NA objective lens (Olympus, LUCPlan FL N) with respective magnifications of 40× and 20× were used for focusing the inscription fs-laser beam at a depth of 170 μm below the top surface of the silica sample. Loose focusing with the 0.4 NA objective with the correction collar intentionally de-tuned to a depth of 0.5 mm was found to be ideal for tuning the physical height of the fabricated waveguides. The inscribing laser power window ranged from 100 to 500 mW, depending on the repetition rate used. The feed rate (scanning velocity) was varied between 0.5 and 4 mm/s. Three different multiscan pitches of 0.2, 0.4, and 0.6 μm were used in this study.

While waveguides written at 100 kHz repetition rates exhibited a positive refractive index change, those waveguides also featured cracks even when the power (energy) was reduced to below 50 mW (50 nJ) under the focusing conditions stated above. An overview of the maximum induced refractive index change measured over the parameter window from 375 kHz to 1 MHz is shown in Fig. 1. As can be seen, waveguides inscribed at a 500 kHz repetition rate with a 1 mm/s feed rate show an almost constant, strong, and smooth index change across the entire power window used, which prevents the formation of laser power fluctuation-induced irregularities along the length of the waveguide. Backscattered electron (BSE) microscope images along with DIC microscope images of the highest index-contrast waveguides obtained for 1 MHz, 750 kHz, and 500 kHz repetition rates are shown in Fig. 2. All waveguides feature a strong negative index change zone sitting on top of the positive index change region. BSE images reveal the morphology of the waveguides, especially in the negative index zone, which was found to be composed of nano-voids. This is a common feature in femtosecond laser inscription due to the strong self-focusing effects attributed to the high peak intensities of the ultrashort laser pulses.[22,23] The nano-voids are surrounded by highly densified shells that can be directly imaged if the polishing happens to end at the right position along the waveguide. Waveguides inscribed at 1 MHz repetition rate tend to show the fewest of such zones, and a detailed explanation of the void-shell morphology can be found in a previous report.[24] The backscattered intensity from the positive index zone under the electron microscope seems constant throughout the area, except for a slight increase in a 1–2 μm wide section at the bottom of the waveguides. It is also interesting to note the slight increase in the lateral width of the waveguides, especially at the transition zone between negative and positive indices.

The BSE image shown in Fig. 3, taken of a single laser-inscribed track with the exact same parameters used for Figs. 2(c) and 2(f),

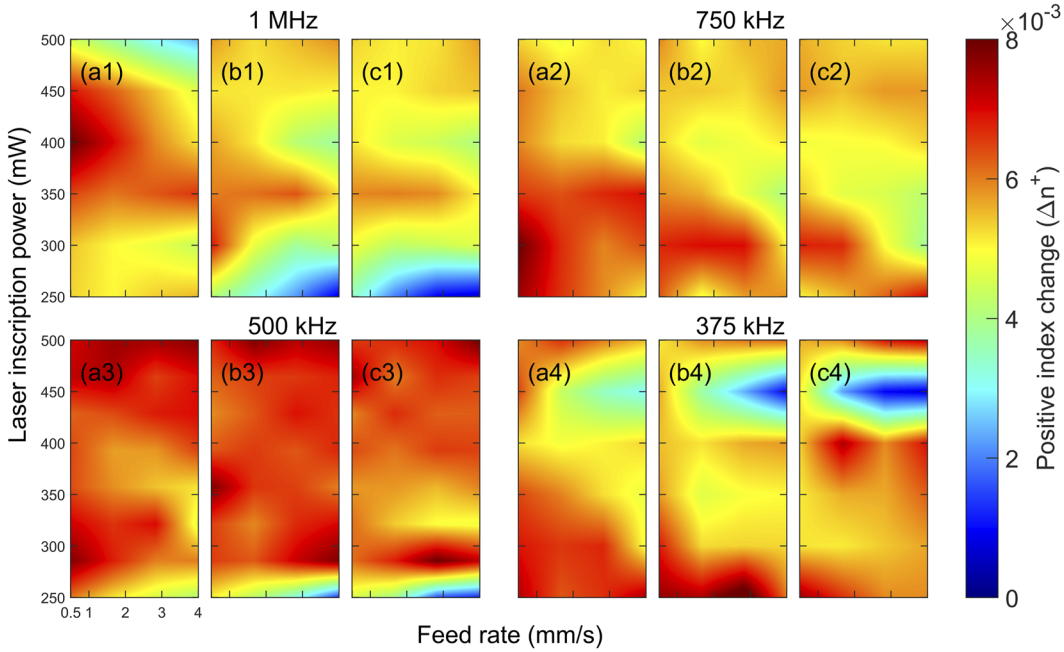

FIG. 1. Maximum positive index change measured for four different repetition rates as a function of feed rate and inscription power. (a1–a4) correspond to a multiscan pitch of 0.2 μm; (b1–b4) to 0.4 μm; and (c1–c4) to 0.6 μm; The total inscription width was kept at a constant 12 μm for all waveguides.

revealed a high aspect ratio inverted tear drop structure that featured a ~3.4 μm broad positive index lobe at the top of the positive index zone, which tapers down to a width of ~0.5 μm (marked with arrows in Fig. 3). This can be attributed to plasma absorption from the aberration profile induced by the de-tuned objective collar.

The losses that are induced by the waveguide inscription process are about 0.6 dB/cm and are largely independent of wavelength over the spectral range investigated. The measured propagation loss for waveguides written at 500 kHz with inscription power and feed rate corresponding to the highest induced index change was found to

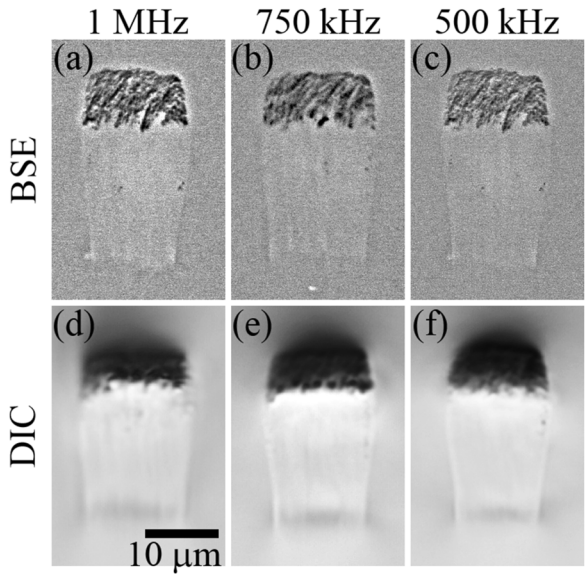

FIG. 2. Backscattered electron (BSE) and Differential Interference Contrast (DIC) microscope images of waveguides written with 450 mW, 1 mm/s, and 0.4 μm pitch for [(a) and (d)] 1 MHz, [(b) and (e)] 750 kHz, and [(c) and (f)] 500 kHz repetition rates, respectively.

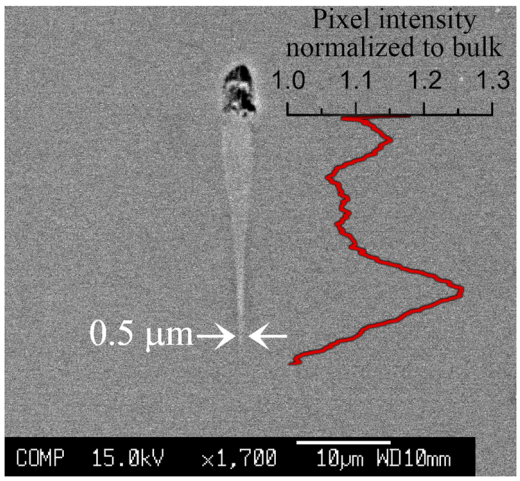

FIG. 3. Backscattered electron microscope images of a single laser-inscribed track written at 500 kHz, 450 mW, and 1 mm/s. Inset: The pixel intensity line profile (normalized to bulk) of the positive index zone within the BSE image.

be 1.1 ± 0.1 dB/cm for all three pitches. From these observations, we chose the 0.4 μm pitch for device fabrication since the 0.6 μm pitch is physically wider than the single structure shown in Fig. 3, and a 0.2 μm pitch would result in longer waveguide fabrication times as compared to the 0.4 μm pitch. While the polarization properties of the waveguides have not been analyzed in detail, multi-scan waveguides are generally known to exhibit weak polarization dependence.

B. Thermal stability and origin of the index change

The laser-inscribed waveguides were subsequently annealed at 400 °C for 15 h. None of them showed any strong physical changes or cracking after annealing. The BSE, DIC, and refractive index profiles of pre-annealed (i.e., non-annealed) and post-annealed waveguides written with 500 kHz, 1 mm/s, 0.4 μm pitch, and 400 mW are shown in Fig. 4. As evident from the BSE images shown in Figs. 4(a) and 4(b), there are no significant density or local stoichiometry changes, nor morphological changes due to the annealing, which is also supported by the DIC microscope images. The refractive index profiles [Figs. 4(c) and 4(d)] show the strongest positive index change at the bottom of the modifications, which is due to densification, as evident from the strong backscattered signal from the same region in Figs. 4(a) and 4(b). It is worth noting that the positive index zones have a step index profile even though the BSE image contrast is weaker as compared to previous reports, especially in silicate glasses.[25] In order to analyze the density and mechanical properties of the waveguides, spatially resolved Brillouin scattering measurements were performed, i.e., the Brillouin frequency shift (BFS) was mapped across the modified and pristine zones. The BFS of pristine Suprasil 3001 glass was measured to be 25.2 GHz (using 660 nm laser excitation), as shown in Fig. 5(a) by the Stokes and anti-Stokes shifts. The BFS in a material depends on the refractive index (n), longitudinal modulus (M), and the physical density (ρ) and is given by the equation $BFS = \frac{2n}{\lambda}\sqrt{\frac{M}{\rho}}$.[26] The refractive index of pristine Suprasil 3001 at 660 nm is 1.4567 and the density is 2200 kg/m^3. From the measured BFS, we deduce the longitudinal modulus to be 71.7 GPa close to the previously reported value of 77.3 GPa[27] in Suprasil 300. 2-D maps of the change in BFS with respect to pristine glass were acquired for pre- and post-annealed waveguides [Figs. 5(b) and 5(c), respectively]. Both of these images clearly show a higher relative shift of about 400 MHz at the bottom of the positive index zone. Since we observe a permanent densification without any signs of fracturing in the waveguides, the material must have undergone a plastic deformation process. Any plastic deformation in silica glass (without additional thermal or shear stress stimuli) is limited by the elastic yield and the saturation pressure to a range between 9 and 25 GPa, resulting in a permanent densification.[27] The BFS is largely insensitive to pressures above (saturation pressure) and below (elastic yield) this range, resulting in sigmoidal behavior overall. The permanent densification region (9–25 GPa) has an almost linear behavior with a 400 MHz per percent density positive slope between those two zones. Within the localized densified zone of the inscribed waveguides, we measured a relative increase in the BFS of 400 MHz and an increase in the refractive

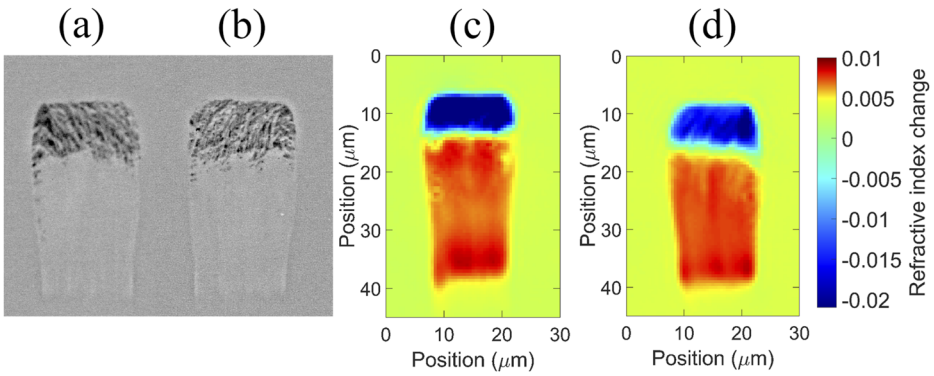

FIG. 4. (a) and (b) BSE, and (c) and (d) refractive index profile cross sections of pre-(left) and post-(right) annealed waveguides written with 500 kHz, 1 mm/s, 0.4 μm pitch, and 400 mW.

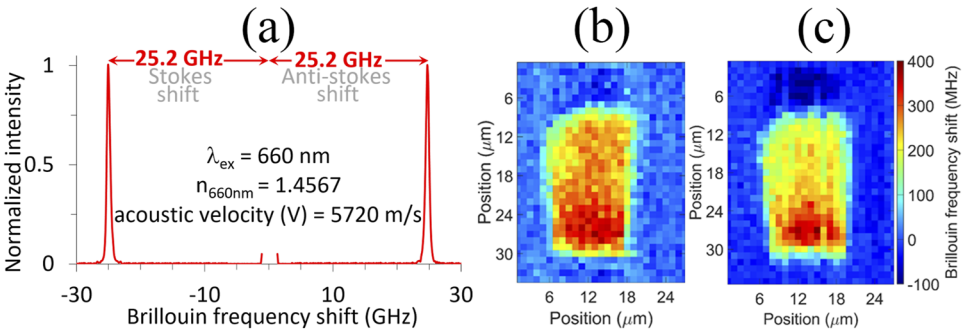

FIG. 5. (a) The absolute Brillouin frequency shift (BFS) spectrum from the pristine glass and the relative BFS map from (b) pre-annealed and (c) post-annealed waveguides, written with 500 kHz, 1 mm/s, 0.4 μm pitch, and 400 mW.

index of 8×10^{-3}. Using the Lorenz–Lorentz model,[28] this change in index can be used to deduce the density change, which is calculated to be ≈1.35% relative increase. This calculation is based on the assumption that the entire index increase is purely caused by densification without any contribution from changes in polarizability within the glass matrix. However, in the case of cold-compressed fused silica,[27] a 400 MHz relative BFS corresponds to only a 1% relative density increase, thus indicating that part of the index increase is caused by other mechanisms.

There is a strong dynamic change in the relative frequency shift of the Brillouin signal in Figs. 5(b) and 5(c) when moving toward the top of the positive index modification, a feature, which is clearly absent in the refractive index profiles. The relative index variation across these two zones is only 10%–20%, whereas the BFS changes by almost a factor of 2. This indicates the presence of open/unfulfilled glass networks that are relatively easier to compress, thus reducing the Brillouin frequency shift in those areas.

The generation of laser-induced defects in fused silica can result in an increase in refractive index through bond-breaking. A non-bridged atom, in this case silicon (Si) or oxygen (O), with an unpaired electron cloud is well known to have a higher polarizability, synonymous with a higher refractive index. Non-bridging oxygen hole centers (NBOHCs) and non-bridging oxygen (NBO) or terminal oxygen exhibit a significantly higher polarizability (3.88 $Å^3$), as compared to bridged oxygen.[29] There are several different paramagnetic defects that are generated through a series of photo-thermo-chemical reactions: SiE′ (terminal silicon with an unpaired bond, ≡ $Si^{\cdot}$), NBOHC (terminal oxygen with an unpaired bond, ≡Si–$O^{\cdot}$), POR (peroxide linkage with an unpaired oxygen bond, ≡Si–O–$O^{\cdot}$), and interstitial oxygen (atom or molecule). Of these, the most investigated defect is the NBOHC, which can be identified relatively easily through Raman microscopy or by observing the luminescence emitted by the electron trap levels set by the defects.

The symmetric stretching vibration of the Si–$O^{\cdot}$ bond in NBOHC was observed and reported in low temperature (<208 °C) photoluminescence (PL) studies, where the zero phonon line and the vibrational peak were found superimposed on the PL and separated by 890 cm^{-1}.[30] Hence, these vibrations are generally accessed through resonant Raman excitations with excitation energies in excess of the bandgap of silica or through the main defect band at 1.9 eV. It was reported that exciting a silica sample containing oxygen excess defects with 325 nm (3.81 eV) light yielded a peak at 890 cm^{-1}, whereas with 442 nm (2.8 eV) excitation, this peak was completely absent. In our case, we excited the sample with 514 nm (2.41 eV) light and were still able to observe this peak, as shown in Fig. 6(a). We believe that ultrafast laser irradiation is efficient enough to produce a distribution of defects, hence setting up diverse trap levels within the forbidden energy gap of silica compared to other linear absorption-mediated or irradiation techniques (x-rays, γ - rays etc.) with energies larger than the bandgap of silica. Such wide defect absorption bands could then explain the "non-resonant" (514 nm) excitation-induced emission seen in our case. A more detailed discussion of this is beyond the scope of this paper.

Raman mapping of the 890 cm^{-1} band for the pre-annealed waveguide [Fig. 6(b)] shows higher intensities at the positive index zones where there was less densification observed in the BSE images. The area at the bottom of the waveguides with strong densification shows no increase in strength of the 890 cm^{-1} band, as highlighted by the white box in Fig. 6(b). The negative index change region is dominated by strong PL corresponding to the defects from cavitation, and hence these regions are masked out. After annealing, a negligible change in index contrast was observed. However, the intensity of the NBOHC symmetric stretching vibration diminishes throughout the entire positive index zone and even drops below the pristine bulk glass, as shown in Fig. 6(c). This indicates that other defects are responsible for the index change. The densified zone at the bottom of the waveguide is a result of an increased population of 3-membered [D_2 band intensity shown in Fig. 6(d)] over the four-membered [D_1 band intensity shown in Fig. 6(e)] Si–O rings. While both the D_1 and D_2 bands increase in intensity,[31] the D_2 peak that corresponds to the three-membered ring agrees well with the observed BFS shown in Figs. 5(b) and 5(c). The gradual reduction in the intensity from left to right of the D_2 peak at the

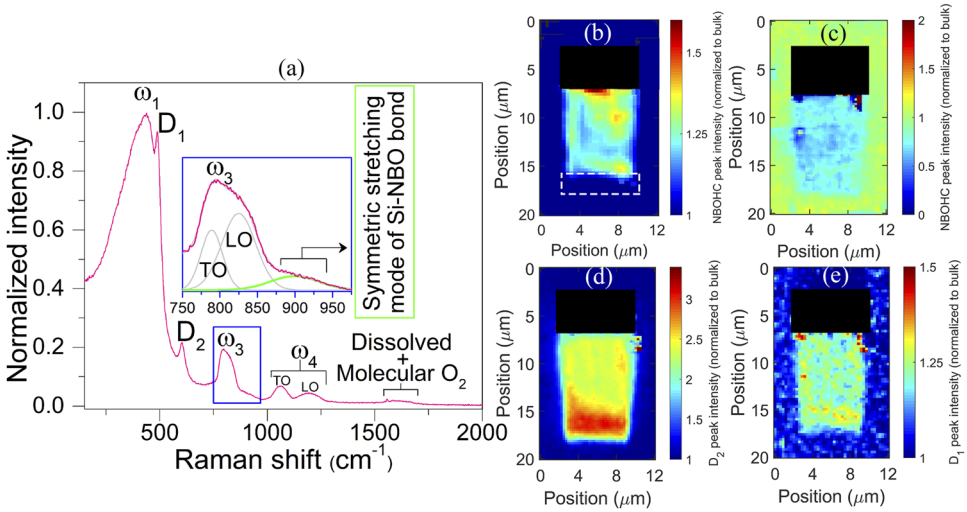

FIG. 6. (a) Raman spectrum of the pristine bulk glass using a 514 nm laser for excitation. The inset shows the shoulder vibrational band corresponding to the symmetric stretching mode at 890 cm^{-1} of NBOHCs along with the transverse-optical and longitudinal-optical split of vibrations due to bridged oxygen in the Si–O–Si network. The intensity of the NBOHC defect band (890 cm^{-1}) mapped across (b) a pre-annealed waveguide and (c) an annealed waveguide. The bottom row shows intensity maps of (d) 3-membered (D_2) and (e) four-membered (D_1) Si–O ring network vibrations. All intensity maps are subtracted from the pristine bulk signal strength.

bottom of the waveguide is mainly caused by laser-induced cumulative stress.[21] The D_2 peak intensity is very sensitive to densification, led by a change in fictive temperature (T_f), which is the temperature at, which the definitive amorphous structure in equilibrium is frozen in when the hot, low viscous glass melt is rapidly quenched. It therefore depends on the rate of cooling, which in turn contributes to the structural density.[32] A linear dependence with a positive slope is reported for the fictive density change; hence, the variation spotted at the bottom of the D_2 peak intensity (which can be translated as the highest temperature achieved) can be attributed to the successive energy deposition in multiscan-writing being progressively affected by the stress within the material, which is left over from the preceding scans.[21] Hence, Fig. 6(d) provides a single integrated image of the energy deposition profile in a multiscan waveguide, which would be almost impossible to generate by using direct imaging techniques.

Since the Raman mapping shows that the NBOHC peak intensity is reduced after annealing but the index change is still preserved, we carried out a detailed investigation of the types of defects generated. The best technique for allowing the examination of the broadest spectrum of defect levels formed within the forbidden bandgap of fused silica is cathodoluminescence (CL). Figure 7(a) shows the CL spectra extracted from pristine bulk and from pixels corresponding to the maximum intensity (irrespective of location) within the pre- and post-annealed waveguide maps. Figures 7(b)–7(d) show intensity maps of pre-annealed waveguides, and (e)–(g) show those of post-annealed waveguides. The signal is clearly intense where the densification is weak, as observed in BSE imaging (Fig. 3) and BFS [Figs. 5(b) and 5(c)] mappings. A white box is shown in the first map to demonstrate the position where the highly densified zone is located within the waveguide region. This particular zone shows a faint increase in intensity for NBOHC defect maps for both pre- and post-annealing [Figs. 7(c) and 7(f)]. A magenta box shows the relative location of the negative index zone in the first map. Most notably, even though NBOHCs [(c) and (e)] show a reduction in intensity following annealing, other types of defects like unpaired silicon [(b) and (e)] and peroxy radicals are still present without much change. Full dynamic bandwidth mapping or an integrated area of deconvoluted peaks of these broad band emissions of all the peaks would provide more details regarding specific index-providing defect types but is beyond the scope of this paper. It has been reported that depending on the type of irradiation (x-ray or γ rays), the annealing temperature has a large variation in removing especially the SiE′ and ≡Si–O–O· (POR) defects in low-OH silica glasses.[33] γ ray-induced SiE′ defects are very stable until 110 °C, and POR defects in fact increase by ~70% (fractional defect population) with annealing until 450 °C before reducing by an order of magnitude every 100 °C for SiE′ and 150 °C for POR. This might explain the wide range of thermal annealing properties reported in the literature for silica waveguides fabricated with ultrafast lasers. The defects created, especially SiE′ and POR, are maintained at least until 400 °C and can be exploited in high-temperature-stable photonic structures. The existence of defects at high temperatures is due to the conversion mechanisms of the defect types, where a weak/highly strained bond is broken and/or an existing defect is rebonded. In our case, it is evident that the observed increase in POR and SiE′ is at the cost of a reduction in NBOHC. This is well in agreement with a previous report by Griscom[33] and also the theoretical calculation of peroxy-radical defects as a stable entity by Edwards and Fowler.[34] Adding to these reports, we have already demonstrated that the unique high positive index change observed in fs-laser-written waveguides in bismuth germanate crystals ($Bi_4Ge_3O_{12}$) is due to the

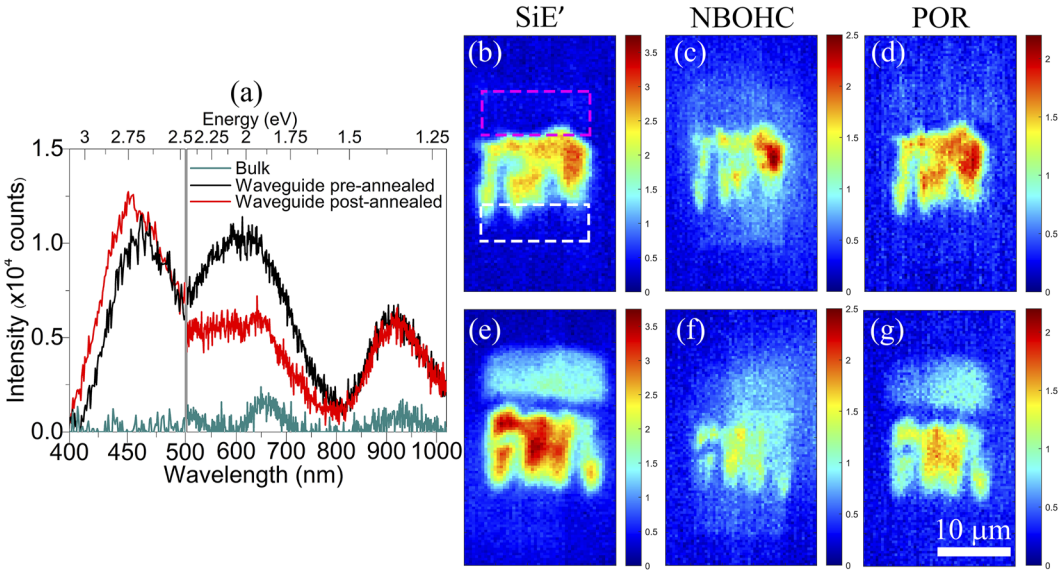

FIG. 7. (a) CL spectra obtained for pristine bulk and pixels corresponding to maximum intensity (irrespective of location) within the pre- and post-annealed maps. Top panels (b)–(d) correspond to pre-annealed waveguides, and bottom panels (e)–(g) correspond to post-annealed waveguides that were written at 500 kHz, 1 mm/s, 0.4 μm pitch, and 400 mW, respectively. The color scale bars are the same for pre- and post-annealed maps, corresponding to the same kind of defects.

high production of peroxy-radicals induced by a significant inward migration of oxygen into the guiding region.[35]

Hence, our results based on the defect type and maximum temperatures clearly call for a more detailed investigation into ultrafast laser-induced defects. The diverse defects induced by various laser parameters and their thermal behavior should be studied further using techniques such as CL and/or UV excitation, which are insensitive to variations in their absorption bands due to thermal annealing.

C. Directional couplers for 3.2 μm wavelength

In order to demonstrate that optimized laser-inscribed waveguides in Suprasil 3001 fused silica glass can be utilized for the fabrication of fiber-pigtailed integrated optical components for the mid-infrared spectral region, directional four-port couplers were designed for operation at a wavelength of 3.2 μm. The free parameters are the arm separation at the input and output end D, the coupling length L, the coupler spacing d, and the total length L_{Device}, as shown in Fig. 8. Enabled by the high index change that can be induced using a 500 kHz repetition rate inscription laser, couplers with very large arm separations (D) and correspondingly small bend radii can be fabricated. This is important from a practical perspective as it allows the couplers to be interfaced to both active and passive single-mode commercial optical fibers. The data sheets available from the leading fluoride fiber manufacturer[36,37] show that single-clad zirconium, indium, or aluminum fluoride fiber diameters range from 123 to 250 (±10) μm. Setting the free parameter D to as wide as 350 μm makes the couplers, thus, physically compatible with all commercially available single-clad fibers. Raised-sine S-bends were used to design the couplers according to the equation

$$y(x) = \frac{D}{S}x - \frac{D}{2\pi}\sin\left(\frac{2\pi}{S}x\right),$$

with a resulting bend radius that can be written as

$$R = \frac{\left[1 + \left(\frac{D}{S}\left(1 - \cos\frac{2\pi}{S}x\right)\right)^2\right]^{\frac{3}{2}}}{\left|\left(\frac{2\pi D}{S^2}\sin\left(\frac{2\pi}{S}x\right)\right)\right|},$$

where x is the longitudinal direction and y is the transverse direction, as indicated in Fig. 8, and S is the side-stepping length along the x-axis over which the S-bend occurs. Larger values for S therefore increase the overall device length but reduce the bend losses. By setting D = 350 μm and S = 3 mm, the radius of curvature is calculated to be 10.4 mm, which is an acceptable value for a high NA waveguide.[38] A series of couplers with different values of d and L were inscribed with 500 kHz, 1 mm/s, 0.4 μm pitch, and 400 mW average laser power. The total insertion loss of all fabricated couplers (sum of the power in both output ports for single input port injection) was measured to be within the range of 1.5–1.9 dB (post-annealing). Given the low waveguide losses as measured for the straight waveguides, increasing the bend radii should result in even lower losses, and a full optimization of the bend radius and device length vs overall insertion loss is subject to further studies.

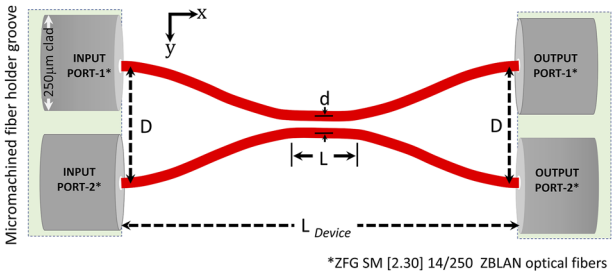

FIG. 8. Schematic of the fabricated symmetric directional four-port couplers, showing the design parameters that are the separation of the input/output ports D, the coupling length L, the waveguide separation d, and the overall device length L_{Device}.

The couplers were characterized using the setup shown in Fig. 8. We have used two different sources, a home-built narrow-linewidth grating-stabilized holmium-praseodymium (Ho/Pr)-doped ZBLAN fiber laser operating at 2.9 μm and a supercontinuum light source (NKT Photonics SuperK) plus narrow band-pass filters (bandwidth 2%) centered at 2.2 and 3.2 μm (Northumbria Optical Coatings), respectively, to investigate the spectral behavior of the couplers. The Ho/Pr laser and the filtered SuperK radiation were both coupled into passive ZBLAN optical fibers (Le Verre Fluore, ZFG SM [2.30] 14/250 fiber) using a ZnSe objective lens with an NA of 0.13 (Edmund Optics, 12 mm FL). These optical fibers were mounted on laser-micromachined grooves that were separated by 350 μm, and the input light was finally fed into input port-1. The input and output fiber grooves were mounted on high-precision 3-axis NanoMax flexure stages. The light was coupled out from both output ports and was detected using a Yokogawa AQ6377 optical spectrum analyzer that covers a wavelength range from 1900 to 5500 nm. Coupler characterizations using the SuperK and Ho/Pr-laser were done without changing the setup. It was found that the couplers were multi-mode at 2.2 μm, while their characteristic at 2.9 and 3.2 μm was virtually identical.

The coupling ratios achieved for different coupling lengths L and waveguide separations in the coupling region d are shown in Figs. 9(a) and 9(b) for pre- and post-annealed waveguides. The measurements were repeated for both input ports, showing variations of only <±3.5% (normalized coupling ratio), thus indicating similar losses between the ports and highly symmetric coupling. These comparative results are shown in Fig. 9 for d = 17 μm. It can also be seen that the beat length increases with waveguide spacing, as expected.

A mode overlap integral (OI) between the waveguide and the fiber mode (fiber type as stated above) of as high as 0.995 was calculated using the following expression:

$$OI = \frac{\left|\iint E_f(x,y)\cdot E_w(x,y)dxdy\right|^2}{\iint |E_f(x,y)|^2 dxdy \iint |E_w(x,y)|^2 dxdy}.$$

Overlapped line profiles of the fiber vs waveguide modes along both axes are provided in Fig. 9(c). The inset shows the 2-D intensity profile of the propagated mode. The transverse cross-sectional mode profiles for different coupling ratios ranging from 5:95 to 50:50 are shown in Fig. 9(d). Given the close to perfect mode-matching, a detailed mathematical analysis of the structure-index-mode analysis, while interesting from a theoretical point of view, is beyond the scope of this paper.

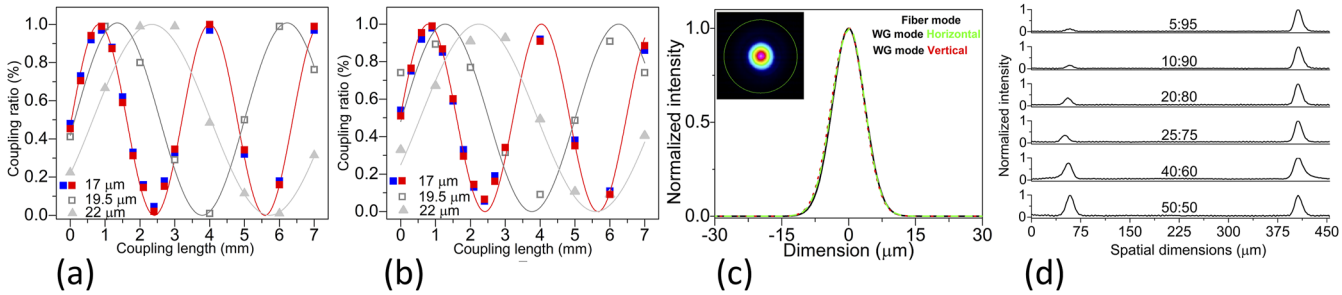

FIG. 9. Coupling ratios obtained for (a) pre-annealed and (b) post-annealed couplers with varying interaction lengths L for 17, 19.5, and 22 μm coupler spacings d. 17 μm coupler spacing has two data points with red and blue colors as they are from repeated measurements from input port-1 and port-2, respectively. (c) Line profiles in comparison to the fiber vs propagated mode through the waveguide. Inset shows the 2D mode profile from one arm of a coupler, depicting the perfectly circular geometry of the propagated mode (d) Different coupling ratios ranging from 5:95 to 50:50 selected from a constant coupler spacing of 17 μm with different coupling lengths.

IV. CONCLUSION

Mid-infrared integrated evanescent four-port couplers operating at 3.2 μm wavelength were demonstrated. The couplers consist of femtosecond laser-inscribed waveguides with a high positive index change and a correspondingly high numerical aperture that is perfectly matched to commercial fluoride optical fibers, thus enabling low-loss fiber pigtailing. Dry fused silica was used as the substrate material, which is an oxide glass that has minimal spectroscopic losses between 2.95 and 3.4 μm wavelength due to its ultra-low OH content. Demonstrating the feasibility of fabricating such an optical element in a thermally and mechanically robust glass, such as fused silica, opens the possibility of designing integrated devices for mid-infrared wavelengths that can operate at high power levels. A comprehensive study of the parameter space for inscribing multiscan optical waveguides in this glass was presented in Sec. III A. This was done by varying the repetition rate (from 100 kHz to 1 MHz), laser power, feed rate, and multiscan waveguide pitch. It was found that waveguides fabricated with a 500 kHz repetition rate exhibited the maximum index change. The origin of the index change that forms the waveguiding region was investigated using Raman and electron microscopy, as well as Brillouin microscopy and cathodoluminescence, two techniques that were introduced here as additional and powerful tools for this purpose. The main mechanisms responsible for the index change were identified as being site-specific densification and changes in highly polarizable units, such as oxygen vacancies attached to a silicon atom and silicon vacancies attached to a peroxide unit. The waveguides were robust and thermally stable at 400 °C for well over 15 h, and the index contrast maintained within the waveguide was still $>1 \times 10^{-2}$. With such a large index change, directional couplers were designed and demonstrated at various coupling ratios ranging from 5:95 to 50:50 operating at 3.2 μm wavelength.

ACKNOWLEDGMENTS

This material is based upon work supported by the Air Force Office of Scientific Research under Award No. FA2386-19-1-4049 as well as by the Australian Department of Defense via the NISDRG funding scheme. This work was performed in part at the OptoFab node of the Australian National Fabrication Facility, utilizing NCRIS and NSW state government funding. The authors acknowledge the use of facilities supported by Microscopy Australia at the Electron Microscope Unit within the Mark Wainwright Analytical Center at UNSW Sydney and helpful discussions with Heraeus Quarzglas GmbH & Co. KG.

AUTHOR DECLARATIONS

Conflict of Interest

The authors have no conflicts to disclose.

Author Contributions

T Toney Fernandez: Conceptualization (equal); Data curation (equal); Formal analysis (equal); Investigation (equal); Methodology (equal); Supervision (equal); Validation (equal); Visualization (equal); Writing – original draft (equal). **B Johnston**: Formal analysis (supporting); Investigation (supporting); Project administration (supporting); Validation (supporting); Writing – review & editing (supporting). **H Mahmodi**: Data curation (supporting); Formal analysis (supporting); Investigation (supporting); Validation (supporting); Writing – review & editing (supporting). **K Privat**: Data curation (supporting); Formal analysis (supporting); Investigation (supporting); Validation (supporting); Writing – review & editing (supporting). **I Kabakova:** Data curation (supporting); Formal analysis (supporting); Funding acquisition (supporting); Methodology (supporting); Resources (supporting); Validation (supporting); Writing – review & editing (supporting). **S Gross**: Data curation (supporting); Formal analysis (supporting); Investigation (supporting); Validation (supporting); Writing – original draft (supporting); Writing – review & editing (supporting). **M Withford**: Formal analysis (supporting); Funding acquisition (supporting); Investigation (supporting); Methodology (supporting); Project administration (supporting); Validation (supporting); Writing – review & editing (supporting). **A Fuerbach**: Conceptualization (equal); Data curation (equal); Formal analysis (equal); Funding acquisition (equal); Investigation (equal); Methodology (equal); Project administration (equal); Resources (equal); Supervision (equal); Validation (equal);

Visualization (equal); Writing – original draft (equal); Writing – review & editing (equal).

DATA AVAILABILITY

The data that support the findings of this study are available from the corresponding author upon reasonable request.

REFERENCES

[1]Y. Fang, Y. Ge, C. Wang, and H. Zhang, "Mid-infrared photonics using 2D materials: Status and challenges," Laser Photonics Rev. **14**, 1900098 (2020).

[2]G. Ycas, F. R. Giorgetta, E. Baumann, I. Coddington, D. Herman, S. A. Diddams, and N. R. Newbury, "High-coherence mid-infrared dual-comb spectroscopy spanning 2.6 to 5.2 μm," Nat. Photonics **12**, 202–208 (2018).

[3]S. Antipov, D. D. Hudson, A. Fuerbach, and S. D. Jackson, "High-power mid-infrared femtosecond fiber laser in the water vapor transmission window," Optica **3**, 1373–1376 (2016).

[4]I. Tiliouine, H. Delahaye, G. Granger, Y. Leventoux, C. E. Jimenez, V. Couderc, and S. Février, "Fiber-based source of 500 kW mid-infrared solitons," Opt. Lett. **46**, 5890–5893 (2021).

[5]G. Stevens and T. Woodbridge, "Mid-IR fused fiber couplers," Proc. SPIE **9730**, 973007 (2016).

[6]M. Rezaei and M. Rochette, "All-chalcogenide single-mode optical fiber couplers," Opt. Lett. **44**, 5266–5269 (2019).

[7]M. Rezaei, M. H. M. Shamim, M. El Amraoui, Y. Messaddeq, and M. Rochette, "Nonlinear chalcogenide optical fiber couplers," Opt. Express **30**, 20288–20297 (2022).

[8]K. M. Davis, K. Miura, N. Sugimoto, and K. Hirao, "Writing waveguides in glass with a femtosecond laser," Opt. Lett. **21**, 1729–1731 (1996).

[9]M. Hughes, W. Yang, and D. Hewak, "Fabrication and characterization of femtosecond laser written waveguides in chalcogenide glass," Appl. Phys. Lett. **90**, 131113-1–131113-3 (2007).

[10]O. M. Efimov, L. B. Glebov, K. A. Richardson, E. Van Stryland, T. Cardinal, S. H. Park, M. Couzi, and J. L. Brunéel, "Waveguide writing in chalcogenide glasses by a train of femtosecond laser pulses," Opt. Mater. **17**, 379–386 (2001).

[11]A. Le Camus, Y. Petit, J.-P. Bérubé, M. Bellec, L. Canioni, and R. Vallée, "Direct-laser-written integrated mid-IR directional couplers in a BGG glass," Opt. Express **29**, 8531–8541 (2021).

[12]J.-P. Bérubé, M. Bernier, and R. Vallée, "Femtosecond laser-induced refractive index modifications in fluoride glass," Opt. Mater. Express **3**, 598–611 (2013).

[13]S. Gross, N. Jovanovic, A. Sharp, M. Ireland, J. Lawrence, and M. J. Withford, "Low loss mid-infrared ZBLAN waveguides for future astronomical applications," Opt. Express **23**, 7946–7956 (2015).

[14]T. T. Fernandez, B. Johnston, S. Gross, S. Cozic, M. Poulain, H. Mahmodi, I. Kabakova, M. Withford, and A. Fuerbach, "Ultrafast laser inscribed waveguides in tailored fluoride glasses: An enabling technology for mid-infrared integrated photonics devices," Sci. Rep. **12**, 14674 (2022).

[15]A. Benoît, F. A. Pike, T. K. Sharma, D. G. MacLachlan, A. N. Dinkelaker, A. S. Nayak, K. Madhav, M. M. Roth, L. Labadie, E. Pedretti, T. A. ten Brummelaar, N. Scott, V. C. du Foresto, and R. R. Thomson, "Ultrafast laser inscription of asymmetric integrated waveguide 3 dB couplers for astronomical K-band interferometry at the CHARA array," J. Opt. Soc. Am. B **38**, 2455–2464 (2021).

[16]J.-P. Bérubé, J. Lapointe, A. Dupont, M. Bernier, and R. Vallée, "Femtosecond laser inscription of depressed cladding single-mode mid-infrared waveguides in sapphire," Opt. Lett. **44**, 37–40 (2019).

[17]J. S. Browder, S. S. Ballard, and P. Klocek, "Physical properties of infrared optical materials," in *Handbook of Infrared Optical Materials*, edited by P. Klocek (CRC Press, 1991), Chap. 4, pp. 141–154.

[18]See https://www.heraeus.com/media/media/hca/doc_hca/products_and_solutions_8/optics/Data_and_Properties_Optics_fused_silica_EN.pdf for Suprasil® 3001 fused silica glass; accessed 20 October 2022.

[19]J.-C. Chanteloup, "Multiple-wave lateral shearing interferometry for wave-front sensing," Appl. Opt. **44**, 1559–1571 (2005).

[20]A. Abou Khalil, W. Gebremichael, Y. Petit, and L. Canioni, "Refractive index change measurement by quantitative microscopy phase imaging for femtosecond laser written structures," Opt. Commun. **485**, 126731 (2021).

[21]Q. Sun, T. Lee, M. Beresna, and G. Brambilla, "Control of laser induced cumulative stress for efficient processing of fused silica," Sci. Rep. **10**, 3819 (2020).

[22]E. N. Glezer and E. Mazur, "Ultrafast-laser driven micro-explosions in transparent materials," Appl. Phys. Lett. **71**, 882–884 (1997).

[23]R. Stoian, "Volume photoinscription of glasses: Three-dimensional micro- and nanostructuring with ultrashort laser pulses," Appl. Phys. A **126**, 438 (2020).

[24]S. Bhardwaj, T. T. Fernandez, S. Gross, M. J. Withford, and M. J. Steel, "Quantitative morphology of femtosecond laser-written point-by-point optical fiber Bragg gratings," Opt. Lett. **47**, 453–456 (2022).

[25]T. T. Fernandez, S. Gross, K. Privat, B. Johnston, and M. Withford, "Designer glasses—Future of photonic device platforms," Adv. Funct. Mater. **32**, 2103103 (2022).

[26]F. Palombo and D. Fioretto, "Brillouin light scattering: Applications in biomedical sciences," Chem. Rev. **119**, 7833–7847 (2019).

[27]T. Deschamps, J. Margueritat, C. Martinet, A. Mermet, and B. Champagnon, "Elastic moduli of permanently densified silica glasses," Sci. Rep. **4**, 7193 (2014).

[28]M. Born and E. Wolf, "Electromagnetic potentials and polarization," in *Principles of Optics*, 6th ed., edited by M. Born and E. Wolf (Pergamon, 1980), Chap. II, pp. 71–108.

[29]N. Zotov, I. Ebbsjö, D. Timpel, and H. Keppler, "Calculation of Raman spectra and vibrational properties of silicate glasses: Comparison between $Na_2Si_4O_9$ and SiO_2 glasses," Phys. Rev. B **60**, 6383–6397 (1999).

[30]L. Skuja, "Time-resolved low temperature luminescence of non-bridging oxygen hole centers in silica glass," Solid State Commun. **84**, 613–616 (1992).

[31]A. Zoubir, C. Rivero, R. Grodsky, K. Richardson, M. Richardson, T. Cardinal, and M. Couzi, "Laser-induced defects in fused silica by femtosecond IR irradiation," Phys. Rev. B **73**, 224117 (2006).

[32]A. K. Varshneya, "Glass transition range behaviour," in *Fundamentals of Inorganic Glasses*, edited by A. K. Varshneya (Academic Press, 1994), Chap. 13, pp. 241–314.

[33]D. L. Griscom, "Defect structure of glasses: Some outstanding questions in regard to vitreous silica," J. Non-Cryst. Solids **73**, 51–77 (1985), part of Special Issue: Glass Science and Technology Problems and Prospects for 2004.

[34]A. H. Edwards and W. B. Fowler, "Theory of the peroxy-radical defect in *a*-SiO_2," Phys. Rev. B **26**, 6649–6660 (1982).

[35]T. T. Fernandez, K. Privat, M. J. Withford, and S. Gross, "Record-high positive refractive index change in bismuth germanate crystals through ultrafast laser enhanced polarizability," Sci. Rep. **10**, 15142 (2020).

[36]See https://leverrefluore.com/products/active-fibers/ for Le Verre Fluoré Fiber solutions; accessed 20 October 2022.

[37]See https://www.fiberlabs.com/products/ for Fiber Labs Inc.; accessed 20 October 2022.

[38]A. Harris and P. Castle, "Bend loss measurements on high numerical aperture single-mode fibers as a function of wavelength and bend radius," J. Lightwave Technol. **4**, 34 (1986).